THE ASTROPHYSICAL JOURNAL, 454:643–653, 1995 December 1

FIRST MAPS OF THE SOFT X-RAY DIFFUSE BACKGROUND FROM THE *ROSAT* XRT/PSPC ALL-SKY SURVEY

S. L. SNOWDEN,[1,2,3] M. J. FREYBERG, P. P. PLUCINSKY,[1,4] J. H. M. M. SCHMITT, J. TRÜMPER, AND W. VOGES
Max-Planck-Institut für Extraterrestrische Physik, D-85740 Garching, Germany
AND
R. J. EDGAR, D. MCCAMMON AND W. T. SANDERS
Department of Physics, University of Wisconsin—Madison, 1150 University Avenue, Madison, WI 53706
Received 1995 March 17; accepted 1995 June 16

ABSTRACT

This paper presents an initial version of the diffuse background results from the *ROSAT* soft X-ray all-sky survey. These maps cover ~98% of the sky in the $\frac{1}{4}$ keV, $\frac{3}{4}$ keV, and 1.5 keV bands, with ~2° angular resolution and high sensitivity for low surface brightness extended features. The effects of non–X-ray contamination and X-rays of solar system origin have been eliminated to the greatest possible extent, but discrete X-ray sources have not been removed. The much improved angular resolution, statistical precision, and completeness of coverage of these maps reveal considerable structure over the entire 0.1–2.0 keV energy range that was not observed previously. The data agree well with previous all-sky surveys in terms of absolute normalization and zero point.

Subject headings: surveys — X-rays: galaxies — X-rays: general — X-rays: ISM

1. INTRODUCTION

The extragalactic diffuse X-ray background was one of the first discoveries in X-ray astronomy (Giacconi et al. 1962), and the existence of Galactic emission below 1 keV was revealed by sounding-rocket experiments in the late 1960s (e.g., Bowyer, Field, & Mack 1968; Henry et al. 1968; Bunner et al. 1969). Surveys with nearly complete sky coverage but modest angular resolution and sensitivity (University of Wisconsin sounding rockets, McCammon et al. 1983; *SAS 3*, Marshall & Clark 1984; *HEAO 1*, Garmire et al. 1992) have since shown that the diffuse X-ray background must be made up of several components and have had considerable impact on our views of intergalactic and interstellar space. Despite this, however, none of these components is yet well determined—or, in some cases, even understood—and we have had only hints of the information that the diffuse X-ray background can potentially provide, particularly about the nature of the interstellar medium in our Galaxy. The complexity and apparent number of components in the diffuse X-ray background require considerably improved angular resolution, modest-to-high spectral resolution, and improved statistical precision for continued progress.

The *ROSAT* XRT/PSPC sky survey was designed to map the sky with high sensitivity for the detection of discrete sources in the 0.1–2.4 keV energy range. It was soon recognized, however, that the telescope and detector parameters chosen for this purpose resulted in an instrument almost ideally optimized for studies of the diffuse background as well. The relatively large effective area and short focal length of the X-Ray Telescope (XRT), coupled with the low-background Position Sensitive Proportional Counter (PSPC) detector, result in an unprecedented signal-to-noise ratio for diffuse-emission studies with an imaging instrument. (At $\frac{1}{4}$ keV, the image is 4 times brighter and the detector background 100 times lower than in the *Einstein* IPC.) The large ~2° field of view and 200 day survey provide about 100 times as many detected photons as in previous surveys, and the imaging system gives more than 100 times better angular resolution, with each photon positioned to $\lesssim 3'$ (although this high resolution was not used in preparing the initial versions of the maps presented in this paper). The uniqueness of this sensitivity to diffuse features in an imaging instrument is emphasized by Table 1, which compares the image-brightness and throughput figures of merit of the *ROSAT* XRT/PSPC with several past and future missions.

The maps presented in this paper were produced without using the position information from the PSPC; the result is an effective angular resolution of ~2°. The pulse heights (X-ray energy information) are divided into three broad bands, which results in overlapping response curves with mean energies near $\frac{1}{4}$ keV, $\frac{3}{4}$ keV, and 1.5 keV. To take full advantage of the angular and energy resolution of the XRT/PSPC requires using an entirely different path through the *ROSAT* data reduction software. Work is well underway on the next version of the maps, which will have an angular resolution of 12′ and which will be divided into seven energy bands to take essentially full advantage of the PSPC's energy resolution. The current maps make use of almost all available survey data and have had charged-particle and solar system X-ray contamination removed with great care, so they embody the full sensitivity and systematic quality of the survey data.

We discuss the survey characteristics and geometry in § 2 and the data reduction, including contamination removal, in § 3. The maps are discussed in § 4 and compared with previous surveys in § 5.

[1] Also Department of Physics, University of Wisconsin—Madison.
[2] Present address: Code 666, NASA/Goddard Space Flight Center, Greenbelt, MD 20771.
[3] Universities Space Research Association.
[4] Present address: Harvard-Smithsonian Center for Astrophysics, 60 Garden Street, Cambridge, MA 02138.

TABLE 1

DIFFUSE SOURCE SENSITIVITY COMPARISON[a]

Comparison Measure	*ROSAT*	*Einstein*	*ASCA*	*SPECTRUM X*	*AXAF*	*XMM*
			Image Brightness[b] (msr)			
277 eV	5.2	1.2	0	1.2	0.2	0.8
700 eV	2.0	0.7	0.5	1.2	0.6	1.7
			Throughput[c] (cm^2 sr)			
277 eV	0.17	0.03	0	0.12	0.005	0.04
700 eV	0.06	0.015	0.003	0.12	0.013	0.09

[a] *ROSAT*: PSPC; *Einstein*: IPC 60′ × 60′ field of view; *ASCA*: SIS (two telescopes); *SPECTRUM X*: SODART + LEPC (two telescopes); *AXAF*: ACIS imaging array (all backside-illuminated CCDs); *XMM*: all CCD imaging (three telescopes).

[b] On-axis effective area × (focal length)$^{-2}$.

[c] Vignetting-corrected effective area × solid angle.

2. DATA

The data presented here were collected during the *ROSAT* (Trümper 1983) all-sky survey (Snowden & Schmitt 1990; Voges 1992) with the Position Sensitive Proportional Counter (Pfeffermann et al. 1987) of the X-Ray Telescope (Aschenbach 1988). The survey was accomplished in four intervals, the dates of which are listed in Table 2. The survey verification and main survey (intervals 1 and 2) were done with the first PSPC. (The XRT was flown with two nearly identical PSPCs; the first was destroyed on 1991 January 25 when the attitude-control system failed and the telescope viewed the Sun.) The two intervals (3 and 4) of survey completion were done with the second PSPC. Before any data selection, there are 10.57×10^6 s of survey time.

2.1. *Survey Geometry*

The geometry of the all-sky survey proved vital to interpretation of the results because the multiple observations of each part of the sky simplified the identification of time periods affected by noncosmic background enhancements. The spacecraft spun about an axis perpendicular to the look direction ("spin axis," normal to the solar panels) once per orbital period, so that a great circle on the sky was observed each orbit (~96 minutes), with a constant scan rate. The great circle included the ecliptic poles because the satellite's spin axis lay in the ecliptic plane, within 15° of the Earth-Sun line. The plane of the great circle precessed by ~4′ each orbit, following the average solar motion. Since the XRT/PSPC field of view is circular with a 57.3 radius, every part of the sky was visible for at least 30 orbits (ignoring data dropouts), or ~2 days, at the ecliptic plane and for the entire survey at the poles. The exposure therefore increases markedly with ecliptic latitude, from a possible maximum of ~700 s at the plane to over 50 ks at the poles. This exposure pattern was modified by observing losses due to passage of the satellite through Earth's radiation belts and the South Atlantic Anomaly (SAA; see Snowden & Schmitt 1990; Snowden et al. 1992). There were additional exposure losses due to satellite and detector problems. The survey-integrated exposure is displayed in Galactic coordinates in an all-sky, equal-area Aitoff projection in Figure 1 (Plate 35). The enhanced exposure toward the ecliptic poles is obvious, as is the exposure variation at constant ecliptic latitude caused by passage through the radiation belts and the SAA.

TABLE 2

SURVEY OBSERVATION INTERVALS

Interval	Dates	*ROSAT* Days
1	1990 Jul 11–1990 Jul 16	41–45
2	1990 Jul 30–1991 Jan 25	60–242
3	1991 Feb 16–1991 Feb 18	263–265
4	1991 Aug 3–1991 Aug 13	435–444

The satellite performed one revolution (spin) each orbit. The look direction was coupled to the orbit in such a way that it was radially outward from Earth whenever the plane normal to the satellite's spin axis passed through Earth's center. (This is the same as Earth's terminator plane rotated around the ecliptic poles by the small offset between the satellite's spin axis and the Earth-Sun line.) This "scan law" minimized the observational zenith angle, which maximized exposure (there was no Earth blockage), reduced the contamination from scattered solar X-rays, and satisfied the atomic oxygen constraint (the angle between the look direction and the velocity vector was required to be greater than 28° to avoid damage to the PSPC's window from impinging atomic oxygen).

The survey geometry required a periodic reversal in the spin direction, called a "scan reversal." To picture the reason for this, consider the view of the orbit from along the Earth-Sun line when the orbital plane is roughly perpendicular to this view. *ROSAT* would be seen to orbit Earth in either a clockwise or a counterclockwise direction, and since the look direction is also approximately perpendicular to this view, it is apparent that the spin direction should be the same so that the telescope is always looking more or less upward, away from Earth. As the orbit precessed, roughly every 35 days the plane of the orbit rotated through the point where it contained the Earth-Sun line. After that point, the sense of the orbit as seeen from along the Earth-Sun line was reversed, e.g., from clockwise to counterclockwise. Thus, the direction of the spin needed to be reversed as well. The scan reversals had the effect of significantly changing the mapping of exposure losses due to the particle belts and the SAA onto the sky, as well as nearly reversing the parts of the sky observed during satellite night (at the antisolar position in the orbit) and satellite day (at the subsolar position). Since the subsolar position at the time of scan reversal also has the worst geometry for scattered solar X-rays, the reversal produces a dramatic "edge" in the projection of this background on the sky.

The scan reversals played a role in the calibration of the scattered solar X-ray background (§ 3.1). A maximum observational zenith angle of 90° was reached at the time of scan

reversal when the satellite was in the ecliptic plane, which produced the maximum intensity of scattered solar X-rays when the satellite was at the subsolar point in its orbit but essentially zero intensity when it crossed the ecliptic plane at night. When the scan rotation was reversed, the look direction at the maximum zenith angle was also reversed, which caused the solar contamination to be projected in the opposite direction on the sky. This allowed a very accurate calibration of the solar background at these times because essentially the same regions of the sky were covered at both maximum and zero contamination.

2.2. *SASS-processed Data*

The data presented in this paper were derived from the Standard Analysis Software System Rev0 (SASS, Gruber 1992; Voges et al. 1992) processing of the survey. The SASS data products were mostly from the TEL processing level, which reduced the data on a 1 *ROSAT* day interval and included the ATTIT (telescope pointing directions), EVRAT (monitor count rates such as the Master Veto, MV), LFTIM (live-time information), and BFLGZ (compressed accepted event information) files. (The start of a *ROSAT* day is defined by the first northward-passing crossing of Earth's equator by the subsatellite point after the last Weilheim ground station contact of a contact cycle, which typically consists of six contacts during six contiguous orbits. *ROSAT* days are thus coupled to the precession of the orbit and are slightly less than 24 hr.) The ORB file is from SAV processing (also on a 1 *ROSAT* day interval), and the accepted times were produced by the OBI processing (on a single-orbit interval). The ORB file contains geometric information, such as the satellite, solar, and lunar positions, on a 60 s basis. The ATTIT file contains the satellite look direction on 1 s intervals. The EVRAT file contains ancillary count-rate data (e.g., the MV count rate) on $\sim$2 s intervals. The LFTIM file contains the live time of the PSPC and has entries only when the live time changes by 1%.

BFLGZ is the principal file and contains the event information. The events are accumulated in 10 s time intervals in the five pulse-height bands whose pulse-height limits are listed in Table 3. For the analysis presented here, we use only the count rate integrated over the entire *ROSAT* XRT/PSPC field of view in bands 2, 3, and 4: the $\frac{1}{4}$ keV, $\frac{3}{4}$ keV, and 1.5 keV bands. The response functions for these bands are displayed in Figure 2.

The raw event amplitudes from the PSPC were used for the BFLGZ processing instead of the gain-corrected, pulse-height invariant (PI) channels. Since the gain of the PSPCs varied during the time intervals included in the survey and was different for the two PSPCs, the normalization of the count rates is made considerably more complicated (see § 3.2). This will not be a problem for the next version of the maps, which will be produced from PI-channel processed data.

TABLE 3

BFLGZ Band Raw Pulse-Height Limits

BFLGZ Band	Channels	Map Band	Scale Factor[a]
1.....	8–11	...	...
2.....	12–49	$\frac{1}{4}$ keV	148.3
3.....	50–91	$\frac{3}{4}$ keV	152.9
4.....	92–201	1.5 keV	166.5
5.....	202–252	...	...

[a] Conversion factor for counts s^{-1} over the field of view to 10^{-6} counts s^{-1} arcmin^{-2}, on-axis. Thus, the units are 10^{-6} counts s^{-1} arcmin^{-2} (counts s^{-1})$^{-1}$.

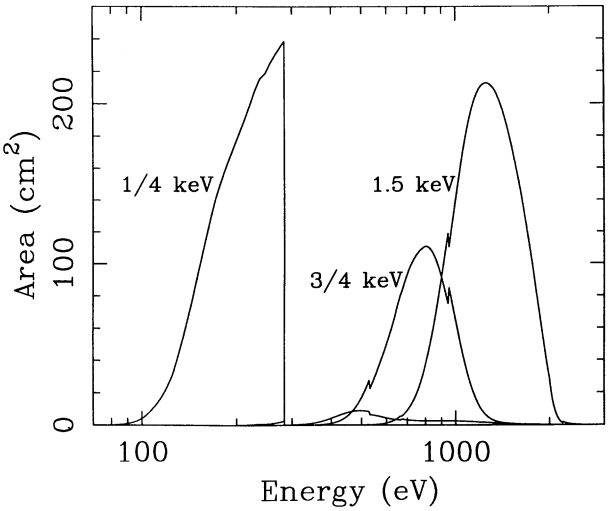

FIG. 2.—Band-response functions for the pulse-height bands used in this analysis.

3. MAP PRODUCTION

3.1. *Noncosmic-Background Exclusion and Modeling*

For a given direction on the sky, from one orbit to the next the pointing of the *ROSAT* XRT/PSPC changed very little compared to the size of the field of view, $\lesssim$4′ versus 115′. Thus, nearly all nonstatistical variations in the count rate from orbit to orbit for a given part of the sky can be attributed to changes in the noncosmic background. We divide the noncosmic background into two categories, the first of which must be removed by excluding intervals of time from the analysis, while the second can be adequately modeled and subtracted from the data. Considerable effort was expended modeling and reducing the noncosmic background of the XRT/PSPC prior to launch (e.g., U. G. Briel 1988, private communication; B. Aschenbach 1988, private communication). The actual background is extensively discussed in Snowden et al. (1994b).

3.1.1. *Identification and Exclusion of Times of Excess Contamination*

We give the label of short-term enhancements (STEs) to the first category of noncosmic-background contamination components. STEs are more readily identified by their temporal signature than by any specific origin. They can last from a few minutes to a few orbits, occasionally with radically varying magnitudes, and can make large contributions to the count rate, often much greater than the soft X-ray background (SXRB). Likely sources include auroral X-rays, enhancements in the scattered solar X-ray background caused by solar flares, and enhanced charged-particle precipitation. X-rays from the Moon when it is in the field of view must also be excluded.

The identification of these contaminated time intervals relied exclusively on the multiple coverage of the survey. An array was created for each of the three bands; each row contained count-rate data from one scan (360°) divided into 180 steps (2° segments), and consecutive rows contained data from consecutive scans. Each element in an array column therefore covered nearly the same segment of sky (2° in ecliptic latitude at nearly constant ecliptic longitude) as its adjacent elements, except that it was shifted by $\lesssim$4′ in ecliptic longitude. The first step in the

analysis of these arrays was to fit a fourth-order polynomial to the data in each column spanning ~10 day (~150 orbit) intervals, after an estimate of the particle background (see below) had been subtracted. The data in each column were then compared to the fitted value, and any element with a greater than 3 σ deviation was excluded and a second fit was performed. A time-ordered sequence of deviations of the data from the second fit, now including the previously excluded elements, was created. The deviations were then combined in sets of 1, 5, and 9 element segments and tested for 5 σ enhancements. If a segment was found to have an excess greater than 5 σ it was flagged to be excluded, along with elements on both sides, for as long as the individual deviations were in excess of 1 σ. This process was moved along on an element-by-element basis through the time-ordered list. After the particle-background time exclusion (see below), this process eliminated an additional 7.5% of the $\frac{1}{4}$ keV data, 2.1% of the $\frac{3}{4}$ keV data, and 0.8% of the 1.5 keV data. In practice, the excluded times derived from the $\frac{3}{4}$ keV data were also excluded from the $\frac{1}{4}$ keV data, which increased the percentage of time excluded from the $\frac{1}{4}$ keV analysis to 8%. The total times included for the maps are 9.43×10^6 s for the $\frac{1}{4}$ keV band, 10.02×10^6 s for the $\frac{3}{4}$ keV band, and 10.15×10^6 s for the 1.5 keV band.

3.1.2. *Modeling and Subtraction of Particle Background*

Since the particle-induced background (PB) of the PSPC is never zero and it routinely varies by a factor of 4 during an orbit, there is no alternative except to model and subtract it from the data. Procedures for the modeling and subtraction of the PB have been the subject of two papers (Snowden et al. 1992; Plucinsky et al. 1993). While these papers were directed more at the analysis of pointed observations, the techniques and calibrations are equally valid and applicable to survey data. Specifically, the models for the temporal and spectral distributions of the PB were adopted directly. The model for the spatial distribution was modified because the SASS processing did not exclude the regions of the PSPCs within the field of view affected by the reduced PB vetoing efficiency near the detector walls. This has a very limited impact on the quality of the data and will be remedied in the final versions of the maps.

We used the published data-selection criterion for the MV count rate (MV < 170 counts s^{-1}) but added another selection criterion as well. As discussed in Snowden et al. (1992), the MV rate is reasonably constant for a given geographic position over Earth. We compared the instantaneous MV rate for all times of the survey with the average MV rate for the geographic position of the satellite. If the MV rate was significantly in excess of the average, which indicates significant deviations from the nominal PB, the time was flagged as bad and not included. This has the advantage of excluding times of abnormal PB in regions where the MV rate was still less than 170 counts s^{-1}. These excess-PB-contamination rejection algorithms excluded 3.1% of the data.

3.1.3. *Modeling and Subtraction of Scattered Solar X-Ray Background*

The scattered solar X-ray background (SB) has also been discussed in detail for XRT/PSPC pointed observations (Snowden & Freyberg 1993; see also Fink, Schmitt, & Harnden 1988). The SB contributes counts, occasionally at rates comparable to or significantly greater than the cosmic background (especially in the $\frac{3}{4}$ keV band), at all times when the Sun-Earth-satellite angle is less than 120°, which is over 75% of the survey. Because of the survey geometry, if a region of the sky was observed during the day, it was most likely observed *only* during the day. A reliable method of modeling and subtracting the SB is, therefore, required since simply excluding the affected times would eliminate considerable sky coverage.

Modeling the geometric variation of the SB is straightforward by use of the simple method of Snowden & Freyberg (1993), as the observed SB is given to good approximation by the product of the solar-illuminated column density along the satellite's viewing direction, the total scattering cross section, and the solar X-ray flux. The illuminated column density is readily calculated from atmospheric models (Jacchia 1972) and the observing geometry. The complication for the survey is the determination of the solar emission. The solar soft X-ray flux and its variation during the survey are unknown a priori since there is no solar X-ray monitor aboard *ROSAT*, nor is there one on any other satellite that was sensitive in the *ROSAT* PSPC bandpass. (*GOES* data contain solar fluxes in the 1.5–12 keV band, which did not prove to be useful in SB modeling or identification.) The survey geometry, however, provides additional tools to retrieve information about the solar X-ray irradiance, which we will briefly describe.

Ecliptic pole regions.—Except during periods of data loss, the north ecliptic pole (NEP) and south ecliptic pole (SEP) were observed every orbit. Since consecutive scan paths over the polar regions are nearly identical (the displacement is $\lesssim 1'$ within 15° of the pole), they can serve as a monitor of total background variation at 48 minute intervals. While variations in the solar flux produce correlated variations at the poles, the coupling between the look direction and orbital position caused the geometric variation in SB contamination (i.e., the variation in the scattering column of the residual atmosphere) at the two ecliptic poles to be negatively correlated (for constant solar flux). Also, the scattering column varied over the regions at the poles and could be used for this analysis. These characteristics provided diagnostics to distinguish variation in the SB from long-term enhancements (see below), which tended to produce similar increases at both poles. Folding all this information together, the excess count rates at the poles were correlated with the computed atmospheric column densities, and a time-dependent conversion factor (equivalent to an estimate of the solar X-ray flux) was derived. In practice, the data losses due to passage of the satellite through the southern radiation belt and the SAA so strongly affected the SEP data that we used only the NEP data for the calculation of the conversion factors.

Scan reversals.—As noted above (§ 2.1), portions of the sky that were observed close to a scan reversal contain a day-night border, i.e., nearly the same part of the sky was observed during both satellite day and night. Subtraction of the nighttime count rates from the daytime count rates yields an SB count rate that again provides a column density–SB conversion factor. The five scan reversals during the survey provide a high-quality calibration since the illuminated column densities are greatest near a scan reversal and the SB contamination often exceeds the cosmic-background count rate.

The Moon.—The Moon came into the field of view at half-phase about twice per month (Freyberg, Schmitt, & Snowden 1995). The folding of the solar soft X-ray flux with the lunar surface-scattering properties are not identical with those of the atmosphere, but the lunar light curve still reflects variations of

the incident solar spectrum. The lunar analysis has, as one main result, shown a strong correlation of the $\frac{1}{4}$ keV count rate with the solar radio flux at 10.7 cm—and thus with solar rotation—while the variations of the $\frac{3}{4}$ keV rate were more affected by isolated events such as flares. We used the 10.7 cm flux to interpolate the $\frac{1}{4}$ keV conversion factor for times between accurate calibration points.

3.1.4. *Identification, Modeling, and Subtraction of Long-Term Enhancements*

The long-term enhancements (LTEs) are the least understood of the background components that must be modeled and subtracted. They are strongest in the $\frac{1}{4}$ keV band, where they occasionally can have intensities comparable to the cosmic background and are present at a level of $\gtrsim 30 \times 10^{-6}$ counts s^{-1} arcmin^{-2} at least 85% of the time. For the most part, they appear to be uncorrelated with parameters such as the geographic subsatellite position, day/night status, geomagnetic latitude, zenith angle, ram angle, and geomagnetic and solar activity. There is a trend that LTEs are on average slightly more intense at greater geomagnetic activity (as measured by the K_P index). However, they also occurred at typical strengths during periods when $K_P = 0$. In no case was there any correlation with a tested parameter that could aid the LTE modeling.

Study of the radial distribution of events in the detector during periods of strong LTE contamination compared to the distribution during relatively LTE-free periods shows no difference in the radial profiles. This indicates that LTE contamination is vignetted *like cosmic X-rays*, which implies a source external to the satellite. Reanalysis of lunar shadowing data presented in Schmitt et al. (1991) shows that the lunar observation occurred during the time of a strong LTE. This was determined by comparing the off-Moon surface brightness in the observation with cleaned survey data from the region. The excess surface brightness from the LTE is consistent with the measured flux from the dark side of the Moon. This suggests that the events contributing to the LTE originate between Earth and the Moon and that there was no emission from the Moon itself. However, the possibility exists that the original explanation for the dark-side events is true and that LTE events originate beyond the Moon in a serendipitous balance.

No physical production mechanism for LTEs has yet been determined, and we have been forced to resort to empirical modeling of the survey count rates for their subtraction. This is not a completely satisfactory method, as it can only address time-variable components with durations of less than ~ 1 week. (See Fig. 7 in Snowden et al. 1994b for an example of the time dependence of LTE contamination.)

The method for identifying the LTEs is similar to that employed for the STEs. Individually for each band, after the modeled PB and SB were subtracted and the times affected by STEs excluded, an array was created, with the rows containing successive scans divided into 20° segments (rather than the 2° segments used for the STE analysis). A running mean count rate for each scan was produced by averaging rates over the 15 rows centered on the scan. Only segments (columns) for which data were available for at least 13 of these scans were included in the average, and sky segments that covered Loop I and the Galactic center region, the LMC, the Eridanus enhancement, the Vela and Puppis supernova remnants, and the Cygnus Loop were excluded to eliminate as much real (cosmic) structure in the data as possible. A spline fit (Press et al. 1986, pp. 86–89) was performed on these running means for the entire survey. A 30 orbit sliding box was then run over the smoothed data to eliminate shorter period fluctuations, and this heavily filtered sequence was searched for minima, which were assumed to be the times of the least (and hopefully zero) LTE contamination. All local minima were taken, except for a few cases in which it was obvious that one was only a temporary dip in a substantial contamination rate.

Next, each column (which represents the same 20° segment on each scan throughout the entire survey) was individually fitted, again using a spline fit. The times of LTE minima (as determined by the method in the previous paragraph) were associated with local minima in the column spline fit. Since the times of the minima determined using the smoothed averages from entire orbits (previous paragraph) were occasionally offset from any minimum in a column fit, the closest minimum in the column fit that lay "downhill" was selected. The minima determined by this process are treated as estimates of the true cosmic X-ray rate for the region of the sky covered by that segment at that time. Because the average cosmic X-ray rate for a segment varies slowly in time because of the slow movement of the segment on the sky, these minima can be connected by interpolation for an orbit-by-orbit estimate of the true rate for each segment. These minima were connected by linear interpolation to form a baseline of equally spaced samples, which was again fitted with a spline to smooth out any sharp, and presumably nonphysical, bends. The interpolated points provided a constraint for the spline fit between the minima to suppress oscillations. This final spline fit produced the "baseline curve," which provides an estimate of the true cosmic X-ray rate for a particular segment of each orbit throughout the survey. The difference between this baseline curve and the spline fit of the column data was then used as an estimate for the LTE contamination count rate for the central time of that segment on each orbit throughout the survey.

After repeating this procedure for all 18 columns, these values for the LTE count-rate estimates for the elements across an individual row are then the estimates for the average LTE count rate for each segment of a given scan. The LTE rate is assumed to vary smoothly with look direction around a scan, so for the final step the estimates for the LTE count rate were assembled in a time-ordered sequence, and linear interpolation was used between the points to determine a continuous (in time) estimate for the LTE rate.

This method has three significant limitations. First, as noted above, it can only eliminate time-variable contamination with a duration of a few days or less. Any relatively constant background component aside from the PB could not be identified and remains in the maps. Second, in regions strongly affected by data losses from passage through the SAA and particle belts, there were insufficient data to determine a baseline, and the modeled contamination was interpolated from as much as 40° away in the scan. Third, the method is effectively a filter for long ($\sim 20°$) linear features aligned with the scan path. It will be confused by (and will tend to remove) real features that accidentally match these characteristics. We identified a small number of such problems by visual inspection of the LTE maps, which were created by projecting the modeled LTE count rates on the sky. In these cases, we eliminated the affected segments from the LTE modeling and interpolated the LTE contamination from neighboring segments.

This procedure is less than satisfying, and perusal of the time history of a typical LTE, as shown in Snowden et al. (1994b),

does not inspire confidence in the supposition that the minima in the LTE rates are truly zeros. Our primary evidence that the cleaning was successful therefore lies in the comparisons made with earlier surveys and discussed in § 5.1. The $\frac{1}{4}$ keV band is by far the most severely affected by LTEs, and the remarkably good agreement in both rates and zero point between this and other $\frac{1}{4}$ keV measurements made at very different times and with entirely different instruments implies that any significant contamination remaining must be constant in time over a period of at least 20 yr. This seems highly unlikely for any source of X-rays related to the solar system.

3.1.5. *Contamination Summary*

Table 4 lists the total number of events in the survey along with the number of modeled background counts for each band. The percentage of modeled background counts compared to the total number of observed counts is 17% for the $\frac{1}{4}$ keV band, 20% for the $\frac{3}{4}$ keV band, and 14% for the 1.5 keV band. As can be seen from Table 4, the most important contamination component is different for each band, with LTEs dominating in the $\frac{1}{4}$ keV band, SB in the $\frac{3}{4}$ keV band, and PB in the 1.5 keV band. Figure 3 shows the fraction of sky affected by contamination at count rates greater than or equal to the specified count rate for the different contamination components for the three bands. This figure clearly shows the different dependencies on the components as a function of energy. Also note that all of the sky is affected by the PB at some level, while ~25% of the sky is unaffected by scattered solar X-rays. (The PB has been multiplied by 10 for both the $\frac{1}{4}$ keV and $\frac{3}{4}$ keV bands for purposes of display. The PB curve for the 1.5 keV band is unscaled.)

3.2. *Map Production*

With all background exclusion and modeling complete, the data in the three bands were projected onto the sky. Exposure times and detected counts minus modeled background counts from the 10 s intervals were accumulated into 40′ × 40′ pixels in two Aitoff equal-area, Galactic-coordinate projections on the sky. For each 10 s interval, all counts and all exposure (live time) were added to the sky pixel containing the center of the field of view at the middle of the interval. No use was made of the count-position information from the PSPC. The count map was divided by the exposure time map to produce a count-rate map.

At the time of the division of the counts by the exposure, the count rates were scaled from the light-bucket count rates in the three BFLGZ bands to effective on-axis count rates in the $\frac{1}{4}$

TABLE 4

NUMBER OF OBSERVED EVENTS AND MODELED BACKGROUND COUNTS: TOTALS FOR THE SURVEY

Component	$\frac{1}{4}$ keV (counts)	$\frac{3}{4}$ keV (counts)	1.5 keV (counts)
Observed Events			
Total[a]	4.953×10^7	1.322×10^7	1.130×10^7
Modeled Background			
LTE	0.651×10^7	0.089×10^7	0.052×10^7
SB	0.168×10^7	0.157×10^7	0.005×10^7
PB	0.032×10^7	0.025×10^7	0.103×10^7
Total	0.851×10^7	0.271×10^7	0.160×10^7

[a] Total number of observed events, cosmic plus contamination.

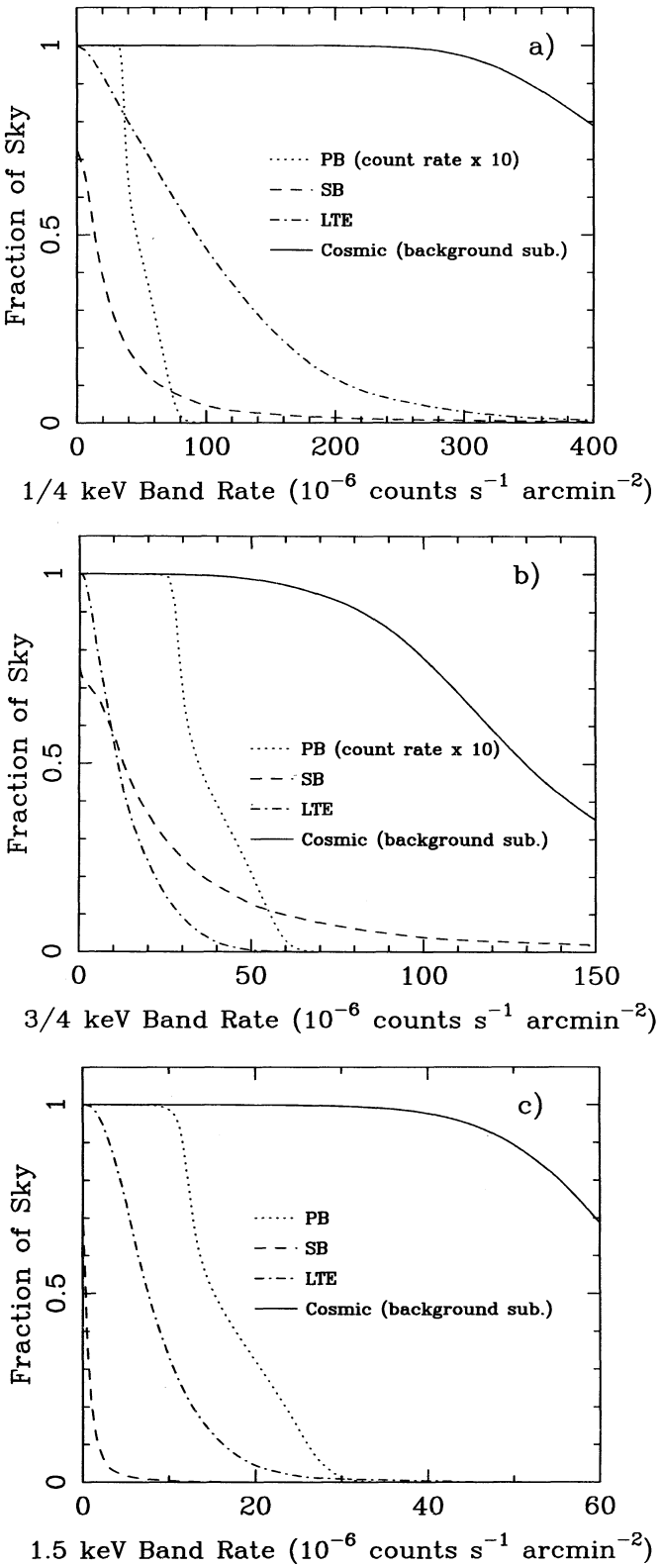

FIG. 3.—Sky fraction as a function of count rate for the different contamination components for the (*a*) $\frac{1}{4}$ keV band, (*b*) $\frac{3}{4}$ keV band, and (*c*) 1.5 keV band. The curves trace out the fraction of sky affected by contamination at a level greater than or equal to the specified count rate. These estimated corrections have been subtracted from the published maps. The low-count-rate parts of the curves for the cosmic background (count rate after the modeled contamination has been subtracted) is shown for comparison.

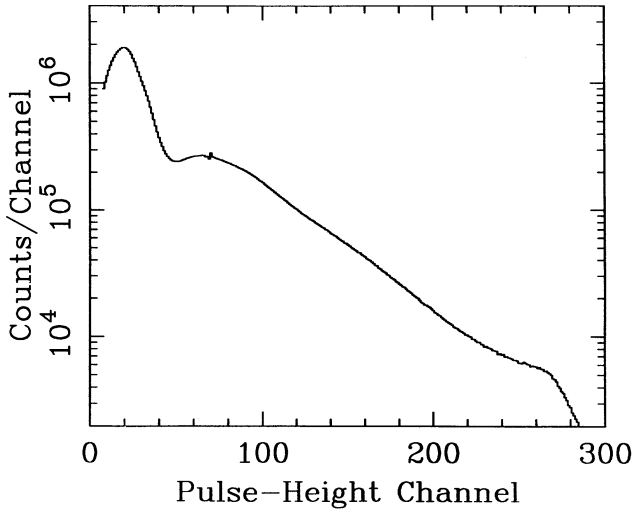

FIG. 4.—Pulse-height distribution in PI channels of survey data. Times of enhanced PB and SB backgrounds have been excluded, as well as times affected by STEs. (There are nominally ~10 eV per channel.) The glitch at channel ~70 is an artifact of SASS processing that has since been corrected, and which has no effect on the maps presented here.

keV band (PI channels 8–41), $\frac{3}{4}$ keV band (PI channels 52–90), and 1.5 keV band (PI channels 91–201; see Snowden et al. 1994b). This was complicated, as mentioned above, by the SASS BFLGZ processing, which used raw pulse heights rather than PI channels. Figure 4 shows the pulse-height distribution in PI channels for the data incorporated in this analysis (data from the SASS SEQ processing). We used this spectrum, after the subtraction of an estimate of the particle background, to derive count-rate correction factors from our raw pulse-height bands to the appropriate constant-energy band in the following manner: For each survey day, we used an interpolated gain measured with the on-board Al Kα calibration sources to find the effective PI-channel band spanned by BFLGZ raw-channel bands. The ratio of the cumulative survey spectrum counts in the standard bands to the cumulative survey spectrum counts in the effective BFLGZ PI-channel bands yielded the desired scale factor.

A scale factor to correct for detector-efficiency variations, including vignetting and obscuration by the window support structure, was required for each band. That is, we need the conversion of counts s^{-1} over the field of view to counts s^{-1} arcmin^{-2}, on-axis. We derived these values, listed in Table 3, from the detector-efficiency maps of Snowden et al. (1994b). The solid angle within the 57.3 radius field of view is 10,315 arcmin^2, which would yield a scale factor of 96.9 (in the same units as the scale factors in Table 3). Comparison of this value to those in Table 3 gives a measure of the reduction in effective area caused by vignetting and obscuration for each band. This varies from 35% for the $\frac{1}{4}$ keV band to 42% for 1.5 keV band.

The final count-rate maps are displayed in Figure 5 (Plates 36–38). While the maps are relatively free of residual structure from noncosmic background, there are several artifacts that can be identified as stripes running parallel to the scan path (at constant ecliptic longitude). Narrow features running parallel to the scan path are thus suspect.

4. DISCUSSION OF THE MAPS

The global structure of the maps is generally similar to that of previous surveys. The major difference lies in the wealth of structure now visible because of the more complete sky coverage, significantly enhanced statistical precision, and improved background rejection and subtraction. The detailed structure in all three bands shows evidence for both emission and absorption variations. Figure 6 shows a diagram identifying many of the brighter and more commonly known features that are discussed in the following sections.

4.1. 1.5 keV *Band*

As in previous surveys, the 1–2 keV band (Fig. 5*a*) is dominated by a relatively isotropic background with discrete Galac-

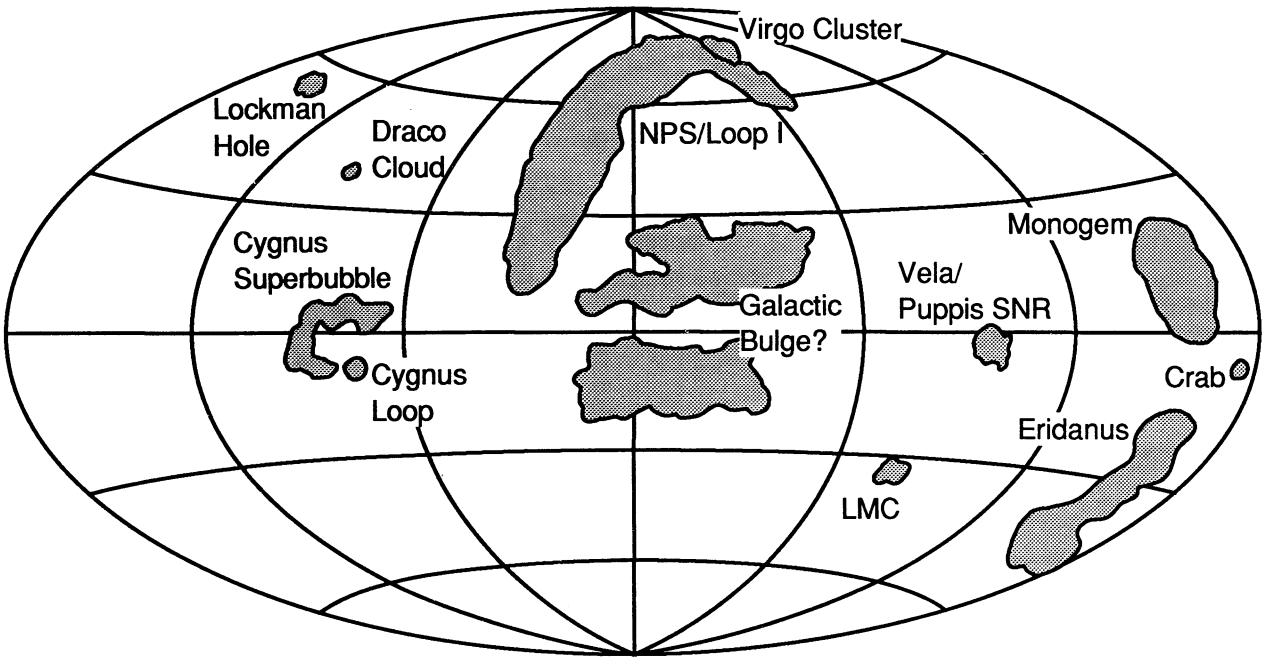

FIG. 6.—Sketch identifying the main features seen in Fig. 5, in the same projection

tic enhancements superimposed. The *ROSAT* survey also shows a distribution of sources at high Galactic latitude (away from the confusion of Galactic emission and absorption by Galactic material) that are likely to be active galactic nuclei and clusters of galaxies, along with discrete sources in the Galactic plane. An apparent absorption feature can be seen that runs along the Galactic plane with varying width from near $l \sim 20°$ through 180° to $l \sim 225°$. Closer to the Galactic center this trough is only a few degrees wide while for $l \gtrsim 100°$ it is up to 10°–20° wide. This appears to reflect the non–plane-parallel distribution of nearby H I in the Galactic anticenter hemisphere.

The brighter and larger extended Galactic sources all show considerable structure. The Cygnus superbubble (the large structure at $l \sim 90°$, $b \sim 0°$) forms a horseshoe opening toward the Galactic center with a low surface brightness extension toward higher latitude/lower longitude. The North Polar Spur is readily apparent, but the interior of Loop I and the Galactic center enhancement form an extensive but confusing distribution of emission without a clear separation of components. The Eridanus enhancement (the large structure at $l \sim 200°$, $b \sim -30°$) appears clearly in this band, with an angular extent similar to that in the $\frac{3}{4}$ keV band (analyzed in Snowden et al. 1995). Typical *IRAS* 100 μm intensities at the north end of the enhancement are ~ 30 MJy sr^{-1} (Wheelock et al. 1994). With the Boulanger & Pérault (1988) conversion factor of 0.86 MJy sr^{-1} (10^{20} H I cm^{-2})$^{-1}$ (appropriate for high-latitude data and so perhaps not completely appropriate for this case), this implies a total column (foreground plus background material) along the line of sight of $\sim 35 \times 10^{20}$ H I cm^{-2}. Since this is only about 1 optical depth in the 1.5 keV band, and the foreground optical depth will be even less, it implies that the Eridanus enhancement is bounded in emission toward the north, rather than being limited by the absorption of intervening material.

4.2. $\frac{3}{4}$ keV *Band*

The $\frac{3}{4}$ keV band (Fig. 5*b*) is generally similar to the 1.5 keV band except that the Galactic features are brighter or, in the case of the absorption features, more pronounced, while the extragalactic contribution is smoother. The Galactic plane absorption feature apparent in the 1.5 keV band now can be traced all the way through the Galactic center enhancement, with considerable structure. The North Polar Spur–Loop I complex and Galactic center enhancement now appear to be more of a small circle on the sky, which suggests a single emission source, i.e., the interior of Loop I. However, the observations are more easily explained by a combination of Loop I and a more distant source—possibly associated with the Galactic bulge. This is apparent when the deep absorption trough running along the Galactic plane is considered. The shape of this trough in the $|b| \lesssim 4°$–10° latitude range is consistent with absorption by the total Galactic H I column. Having the required column density (very roughly, about 5×10^{21} cm^{-2}) between us and Loop I, the center of which is believed to be only about 170 pc away, seems unlikely, but detailed models need to be constructed to verify this.

4.3. $\frac{1}{4}$ keV *Band*

The $\frac{1}{4}$ keV band (Fig. 5*c*), as in previous surveys, shows completely different angular structure than the higher energy bands. Where the higher energy maps are essentially isotropic with the superposition of Galactic features, the $\frac{1}{4}$ keV band shows structure over the entire sky with a strong Galactic plane-to-pole variation. As discussed extensively in the past (see McCammon & Sanders 1990 for a recent review), the negative correlation with the column density of Galactic neutral hydrogen has always been suggestive of the absorption of a flux of extragalactic or Galactic halo origin. However, for a number of reasons, global models using absorption of isotropic, plane-parallel, or other smoothly varying distant components to generate all of the observed negative correlation failed to provide good fits to the data (e.g., McCammon et al. 1983). Before *ROSAT* observations, the model of the $\frac{1}{4}$ keV background in greatest agreement with all of the relevant data had the bulk of the observed emission originating in the Local Hot Bubble (LHB), with the variation in intensity attributed to variation in the radius of the bubble and, therefore, emission measure (Snowden et al. 1990).

ROSAT observations have shown the origin of the $\frac{1}{4}$ keV background to be considerably more complicated than simple emission from the LHB. There is strong evidence for $\frac{1}{4}$ keV X-ray emission in at least the lower halo ($z > 200$ pc) in the direction of Draco (Burrows & Mendenhall 1991; Snowden et al. 1991), Ursa Major (Snowden et al. 1994a), and the M complex of high-velocity clouds (Herbstmeier et al. 1995). However, the halo emission must be rather patchy since the halo emission measure in the direction of the N_H minimum in Ursa Major, $\sim 40°$ distant on the sky from Draco, is considerably lower (an order of magnitude) than that for Draco (Snowden et al. 1994a). Deep surveys at high Galactic latitudes (e.g., Hasinger et al. 1993) have resolved numerous extragalactic sources emitting in the $\frac{1}{4}$ keV band. With the relatively limited survey exposure, these sources provide an unresolved extragalactic "diffuse" component, which can contribute up to $\sim 12\%$ of the observed $\frac{1}{4}$ keV flux in certain low-N_H directions (Snowden et al. 1994a).

What is apparent in *ROSAT* data (both survey and pointed observations) and the maps presented here, which was not previously observed, is the wealth of detailed structure. This structure, when compared to maps of Galactic N_H, shows an almost ubiquitous negative correlation between the two data sets (e.g., Snowden 1993; Burrows & Mendenhall 1994). However, the depth of the X-ray shadows and the brightness of the X-ray maxima are not commensurate with the variation of H I column density (assuming a smoothly distributed flux of distant origin). A specific example is that the region of minimum Galactic N_H is not the direction of maximum X-ray intensity. The simplest explanation for this lack of rigorous, global, negative correlation is that (1) the local component of the $\frac{1}{4}$ keV background contributes a large fraction of the observed background and varies significantly (with a dynamic range of at least 2.5), increasing generally from plane to pole (see Snowden 1993) in agreement with Snowden et al. (1990), while (2) halo and extragalactic components exist with the halo emission showing strong variations (at least an order of magnitude) across the sky.

This still leaves the long-standing problem of the apparent lack of color variations that should be produced by interstellar absorption (see McCammon & Sanders 1990 for an extensive discussion). However, the next version of the *ROSAT* diffuse-background maps will have the $\frac{1}{4}$ keV band divided into two parts. The energy discrimination is not great, but the high statistical precision and uniform data quality should allow this color problem to be studied much more thoroughly than was previously possible.

5. COMPARISON OF THE *ROSAT* MAPS WITH PREVIOUS SURVEYS

As we have seen, contamination removal is a complicated and sometimes uncertain task. Response calibrations of X-ray instruments are also difficult. Because of a paucity of appropriate standard cosmic sources for in-flight calibration, the absolute response functions are usually determined through a combination of separate laboratory measurements on different components of the system and calculated efficiencies. These response functions are then compared by use of the limited sample of astrophysical objects with stable and well-determined intensities. Diffuse response calibrations are further complicated by the necessity of determining a multidimensional response that gives the effective area as a function of X-ray energy, accepted pulse heights, and off-axis and azimuthal angles. The best method we have for checking on the degree of success in cleaning the data and on the accuracy of the calibration is to compare the results with independent surveys.

There are three existing all-sky surveys that have mapped the diffuse X-ray background in the energy range covered by *ROSAT*. These are from a series of Wisconsin sounding-rocket flights (McCammon et al. 1983), *SAS 3* (Marshall & Clark 1984), and *HEAO 1* (Garmire et al. 1992). These surveys were performed at different times with very different instruments that were calibrated independently by different groups. While none of them comes close to the angular resolution or statistical precision of the *ROSAT* survey, all have adequate precision when averaged over modest areas on the sky. We compare each of these surveys with the *ROSAT* survey results by dividing the sky into $22.^{\circ}5 \times 15^{\circ}$ pixels and finding the average rate within each pixel ($10^{\circ} \times 10^{\circ}$ pixels were used for the *HEAO 1/ROSAT* comparisons, where the counting statistics on both missions justified the smaller bins). Parts of the sky with high-contrast, sharp-edged features, such as Loop I and the Eridanus and Cygnus superbubbles, were excluded from the comparison because of the very different angular resolutions of the different surveys.

5.1. $\frac{1}{4}$ keV *Band*

We have compared the *ROSAT* $\frac{1}{4}$ keV band with the *SAS 3* survey, the C band from the Wisconsin survey, and the maximally cleaned 0407 band from *HEAO 1* (maps f/ef0.0407.max on the Penn State distribution tape). Figures 7*a*–7*c* show scatter plots for the three comparisons. All six possible comparisons among these four surveys were fitted simultaneously for a consistent set of slopes and zero offsets, and the results are given in Table 5 with their 1 σ statistical uncertainties. Although bright point sources and high-contrast features can give incorrect results on some pixels, we have attempted to avoid biasing the results by excluding only a small number of obvious extreme outliers from the fit. The excluded points are plotted as squares in the figures; a few others were outside the range of these plots.

We are particularly concerned with the zero offsets in this band, since the poorly understood LTE background is by far the strongest here, and we have no assurance that its removal was complete (see § 3.1). It is very comforting, therefore, to see that all the offsets are small compared to the $\sim 300 \times 10^{-6}$ counts s^{-1} arcmin^{-2} rates typical in the fainter regions at low Galactic latitudes. The *ROSAT* and Wisconsin zero points are in particularly good agreement, and the relative excess in the

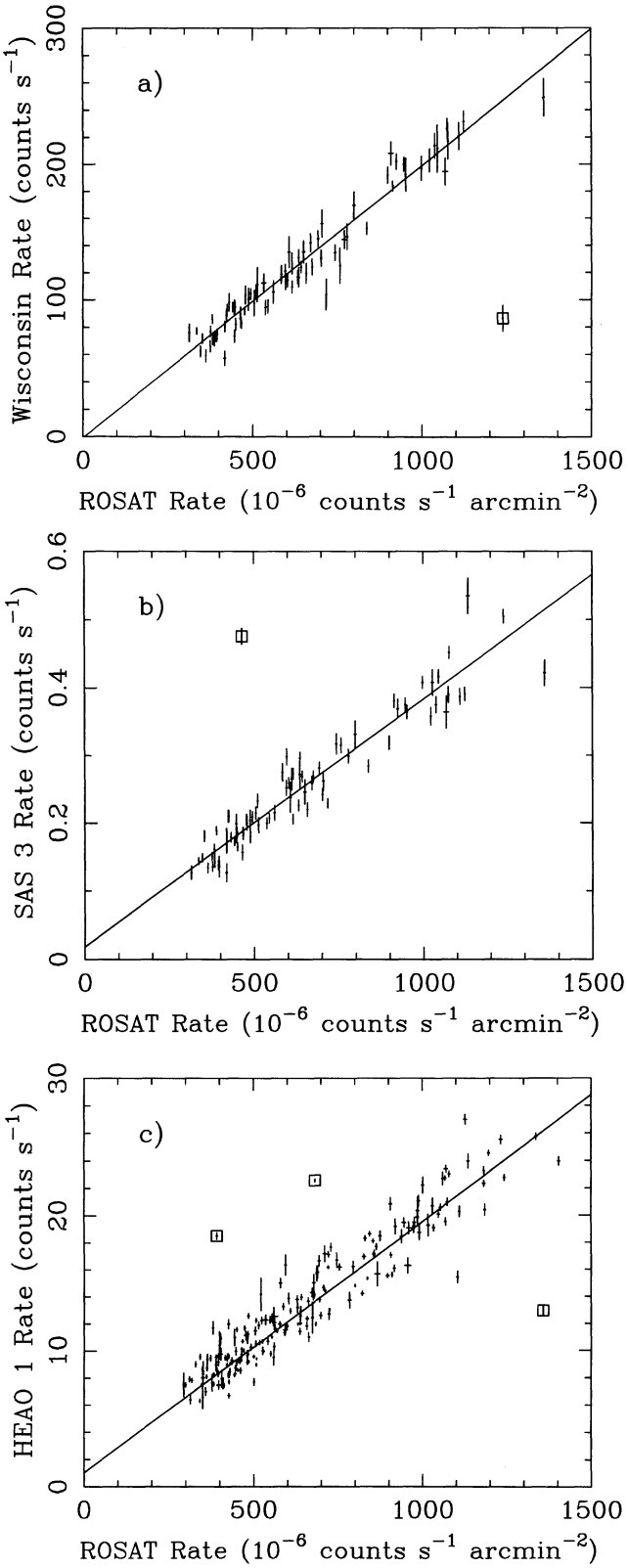

FIG. 7.—Scatter plot of (*a*) Wisconsin C band, (*b*) *SAS 3* C band, and (*c*) *HEAO 1* $\frac{1}{4}$ keV band data versus *ROSAT* $\frac{1}{4}$ keV band data, binned in ~ 340 deg^2 pixels (~ 100 deg^2 pixels for [*c*]). Data points eliminated from the correlation analysis are indicated by squares (a few others lie outside the ranges covered by the plots). The extent of the symbols shows the ± 1 σ error bars for the data.

TABLE 5

CORRELATION OF *ROSAT* DATA WITH PREVIOUS SURVEYS

Survey	Fitted Slope	Offset[a]	Predicted Slope	Difference[b] (%)
		$\frac{1}{4}$ keV Band		
Wisconsin/*ROSAT*.....	0.200 ± 0.005	-5 ± 15	0.186	+8
HEAO 1/*ROSAT*.....	0.0185 ± 0.0001	55 ± 8	0.0167	+11
SAS 3/*ROSAT*.....	$(3.65 \pm 0.07) \times 10^{-4}$	50 ± 11	3.38×10^{-4}	+8
		$\frac{3}{4}$ keV Band		
Wisconsin/*ROSAT*.....	0.390 ± 0.003	0	0.390	0
HEAO 1/*ROSAT*.....	0.0308 ± 0.0001	0	0.0299	+3
		1.5 keV Band		
Wisconsin/*ROSAT*.....	0.581 ± 0.003	0	0.544	+7
HEAO 1/*ROSAT*.....	0.0169 ± 0.0001	0	0.167	+1

[a] The y-intercept of the straight-line fit in Fig. 7 divided by the slope to express it in *ROSAT* count-rate units (10^{-6} counts s^{-1} $arcmin^{-2}$). This has been forced to be zero for the $\frac{3}{4}$ keV and 1.5 keV band fits.

[b] Percentage by which the fitted slope exceeds the value predicted using the published instrument-response functions.

other two surveys can reasonably be attributed to residual soft-electron contamination since these instruments did not have the protection from low-energy electrons afforded by either the low altitude of the sounding-rocket survey or the well-baffled, long–focal-length optics of *ROSAT*. If there is any significant remaining contamination from the LTEs, it must be constant in time.

We can use the fitted slopes from Table 5 to check the accuracy of the effective-area function derived from the *ROSAT* calibrations. Since the shape of the effective area versus energy band response curve is somewhat different for each of the instruments, the predicted ratios have a weak dependence on the assumed input spectrum. We obtain a spectrum to use for the comparisons by choosing a power law with an index that gives the ratio of B-band to C-band rates observed by the Wisconsin survey. This ratio is much more sensitive to the input spectrum than any of the comparisons in Table 5, as can be seen from the predicted ratios plotted against power-law index in Figure 8. (The *HEAO 1* and *ROSAT* $\frac{1}{4}$ keV bands are almost identical, so this ratio is nearly independent of the input spectrum.) The survey ratios predicted using this spectrum are also given in the table and are all about 10% less than the observed values. (A comparison using Raymond & Smith 1977 thermal spectra, 1984 vintage, at a temperature of $10^{6.0}$ K—as determined by the B/C ratio—gives essentially the same predictions.) The agreement among the three older surveys is excellent, as noted previously by McCammon & Sanders (1990), so the results suggest that the effective area for the *ROSAT* $\frac{1}{4}$ keV band is about 10% high.

5.2. $\frac{3}{4}$ keV *and* 1.5 keV *Bands*

Similar comparisons were made for the $\frac{3}{4}$ keV and 1.5 keV bands. For the $\frac{3}{4}$ keV band, we compared the Wisconsin M band (M1 + M2) and used a combination of the *HEAO 1* 1216 band plus 0.4 times the 1921 band to get a better approximation of the *ROSAT* $\frac{3}{4}$ keV energy response. For comparison with the 1.5 keV band, we used the Wisconsin I band plus 0.4 times the J band and 0.9 times the 1921 band plus 1.5 times the 2426 band for *HEAO 1*. (The *SAS 3* survey has only the $\frac{1}{4}$ keV band.) At these energies, there is insufficient range in the observed rates to obtain meaningful values for the zero intercepts, so all offsets were assumed to be zero. This should not be a serious problem, since the backgrounds are much better understood and can be corrected reliably in these bands. We again used power-law spectra to predict the expected rate ratios, fixing the index at -2.31 for the $\frac{3}{4}$ keV band using the observed Wisconsin M1/M2 ratio (0.635 ± 0.011) and at -1.89 for the 1.5 keV band using the observed Wisconsin I/J band ratio (0.657 ± 0.007). The predicted ratios between the surveys are given in Table 5. The agreement for the $\frac{3}{4}$ keV band is excellent, as is the *ROSAT*/*HEAO 1* comparison for the 1.5 keV band. The Wisconsin survey appears to be about 7% high in this band, which is consistent with their estimated systematic-error limits but might also be explained by the low-energy tail on the Wisconsin response curve, which would pick up some of the Galactic thermal emission.

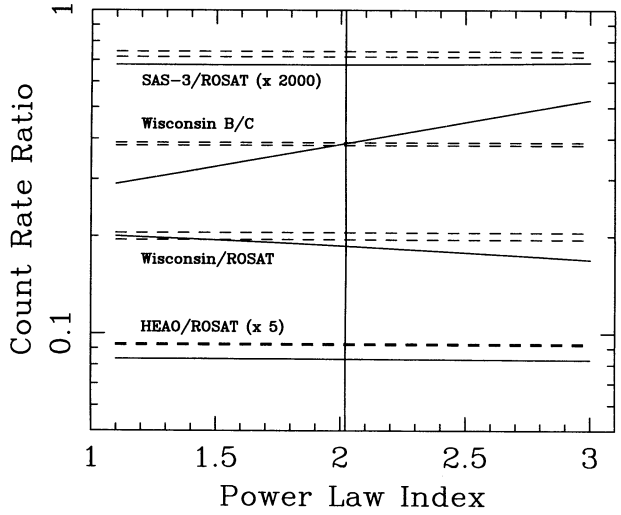

FIG. 8.—Model curves showing the expected ratios of count rates in the different $\frac{1}{4}$ keV bands as a function of power-law index for an assumed unabsorbed power-law spectrum. The pairs of horizontal dashed lines are the ± 1 σ limits of the slopes fitted to the scatter plots in Fig. 7. The vertical line shows the power-law index determined by use of the Wisconsin C/B band ratio.

Overall, the agreement between these surveys is excellent, lending considerable confidence to both the calibration accuracy and the contamination removal.

6. CONCLUSIONS

We have presented new maps of the soft X-ray diffuse background derived from the *ROSAT* all-sky survey. The data have been cleaned of noncosmic-background contamination and corrected for exposure and vignetting. They provide the highest resolution, highest sensitivity images of the sky in the 0.1–2.0 keV energy range ever available.

The absolute normalizations, both zero levels and scale factors, are in reasonable agreement with previous surveys for all energy bands. However, the results suggest that the published effective area for the $\frac{1}{4}$ keV band may be too large by $\sim 10\%$.

The images display the same general morphology observed in previous surveys but, with the better resolution, show considerably more detailed structure. The next version of the *ROSAT* maps to be published will be divided into seven energy bands with 12′ angular resolution and will have point sources removed to a uniform flux level. These maps should allow a wide variety of sensitive, quantitative studies to be made.

The *ROSAT* project was supported by the Bundesministerium für Forschung und Technologie (BMFT/DARA) and the Max-Planck-Gesellschaft (MPG). These maps could, of course, never have been produced without the work of a large number of people: our colleagues at MPE who built and operated the XRT/PSPC and those who produced the SASS software. We would also like to thank our colleagues in Wisconsin for many long and fruitful discussions about the data reduction for the all-sky survey. This research was supported in part by the National Aeronautics and Space Administration under grants NAG 5-629, NAG 5-1438, NAG 5-1817, DARA and the Max Planck Institute for Extraterrestrial Physics.

REFERENCES

Aschenbach, B. 1988, Appl. Opt., 27, 1404
Boulanger, F., & Pérault, M. 1988, ApJ, 330, 964
Bowyer, C. S., Field, G. B., & Mack, J. E. 1968, Nature, 217, 32
Bunner, A. N., Coleman, P. L., Kraushaar, W. L., McCammon, D., Palmieri, T. M., Shilepsky, A., & Ulmer, M. 1969, Nature, 223, 1222
Burrows, D. N., & Mendenhall, J. A. 1991, Nature, 351, 629
———. 1994, in AIP Conf. Proc. 313, The Soft X-Ray Cosmos, ed. E. M. Schlegel & R. Petre (New York: AIP), 16
Fink, H. H., Schmitt, J. H. M. M., & Harnden, F. R., Jr. 1988, A&A, 193, 345
Freyberg, M. J., Schmitt, J. H. M. M., & Snowden, S. L. 1995, in preparation
Garmire, G. P., Nousek, J. A., Apparao, K. M. V., Burrows, D. N., Fink, R. L., & Kraft, R. P. 1992, ApJ, 399, 694
Giacconi, R., Gursky, H., Paolini, F. P., & Rossi, B. B. 1962, Phys. Rev. Lett., 9, 439
Gruber, R. 1992, in Data Analysis in Astronomy IV, ed. V. Di Gesù et al. (New York: Plenum), 153
Hasinger, G., Burg, R., Giacconi, R., Hartner, G., Schmidt, M., Trümper, J., & Zamorani, G. 1993, A&A, 275, 1
Henry, R. C., Fritz, G., Meekins, J. F., Friedman, H., & Byram, E. T. 1968, ApJ, 153, L11
Herbstmeier, U., Mebold, U., Snowden, S. L., Hartmann, D., Burton, W. B., Moritz, P., Kalberla, P., & Egger, R. 1995, A&A, 298, 606
Jacchia, L. G. 1972, in CIRA 1972, compiled by The Committee for CIRA of COSPAR Working Group 4 (Berlin: Akademie), 227
Marshall, F. J., & Clark, G. W. 1984, ApJ, 287, 633
McCammon, D., Burrows, D. N., Sanders, W. T., & Kraushaar, W. L. 1983, ApJ, 269, 107
McCammon, D., & Sanders, W. T. 1990, ARA&A, 28, 657
Pfeffermann, E., et al. 1987, Proc. SPIE, 733, 519
Plucinsky, P. P., Snowden, S. L., Briel, U. G., Hasinger, G., & Pfeffermann, E. 1993, ApJ, 418, 519
Press, W. H., Flannery, B. P., Teukolsky, S. A., & Vetterling, W. T. 1986, Numerical Recipes (Cambridge: Cambridge Univ. Press)
Raymond, J. C., & Smith, B. W. 1977, ApJS, 35, 419
Schmitt, J. H. M. M., Snowden, S. L., Aschenbach, B., Hasinger, G., Pfeffermann, E., Predehl, P., & Trümper, J. 1991, Nature, 349, 583
Snowden, S. L. 1993, Adv. Space Res., 13(12), 103
Snowden, S. L., Burrows, D. N., Sanders, W. T., Aschenbach, B., & Pfeffermann, E. 1995, ApJ, 439, 399
Snowden, S. L., Cox, D. P., McCammon, D., & Sanders, W. T. 1990, ApJ, 354, 211
Snowden, S. L., & Freyberg, M. J. 1993, ApJ, 404, 403
Snowden, S. L., Hasinger, G., Jahoda, K., Lockman, F. J., McCammon, D., & Sanders, W. T. 1994a, ApJ, 430, 601
Snowden, S. L., McCammon, D., Burrows, D. N., & Mendenhall, J. A. 1994b, ApJ, 424, 714
Snowden, S. L., Mebold, U., Hirth, W., Herbstmeier, U., & Schmitt, J. H. M. M. 1991, Science, 252, 1529
Snowden, S. L., Plucinsky, P. P., Briel, U., Hasinger, G., & Pfeffermann, E. 1992, ApJ, 393, 819
Snowden, S. L., & Schmitt, J. H. M. M. 1990, Ap&SS, 171, 207
Trümper, J. 1983, Adv. Space Res., 2(4), 241
Voges, W. 1982, in Proc. Satell. Symp. 3, Space Science with Particular Emphasis on High-Energy Astrophysics, ed. T. D. Guyenne & J. J. Hunt (Noordwijk: ESA), 9
Voges, W., et al. 1992, in Proc. Satell. Symp. 3, Space Science with Particular Emphasis on High-Energy Astrophysics, ed. T. D. Guyenne & J. J. Hunt (Noordwijk: ESA), 223
Wheelock, S., et al. 1994, *IRAS* Sky Survey Atlas Explanatory Suppl. (JPL Publ. 94-11; Pasadena: JPL)

1995ApJ...454..643S

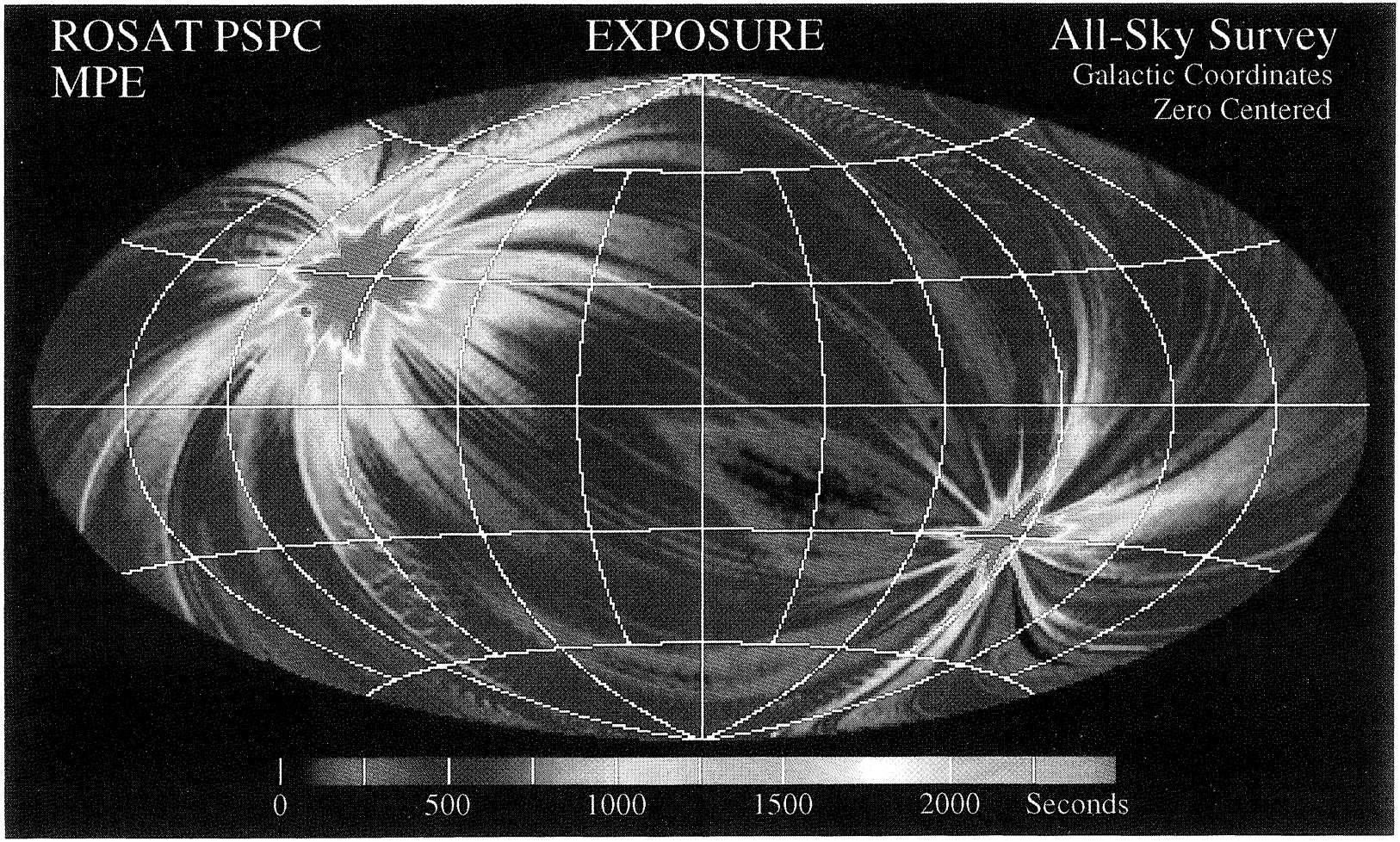

FIG. 1.—Survey exposure for the 1.5 keV band in zero-centered Galactic coordinates with an Aitoff equal-area projection. Units are seconds. The exposure is for one resolution element, which is the detector field of view (57.3 radius). The data have been corrected for dead time but not for vignettting and shadowing of the field of view by the window support structure.

SNOWDEN et al. (see 455, 644)

PLATE 35

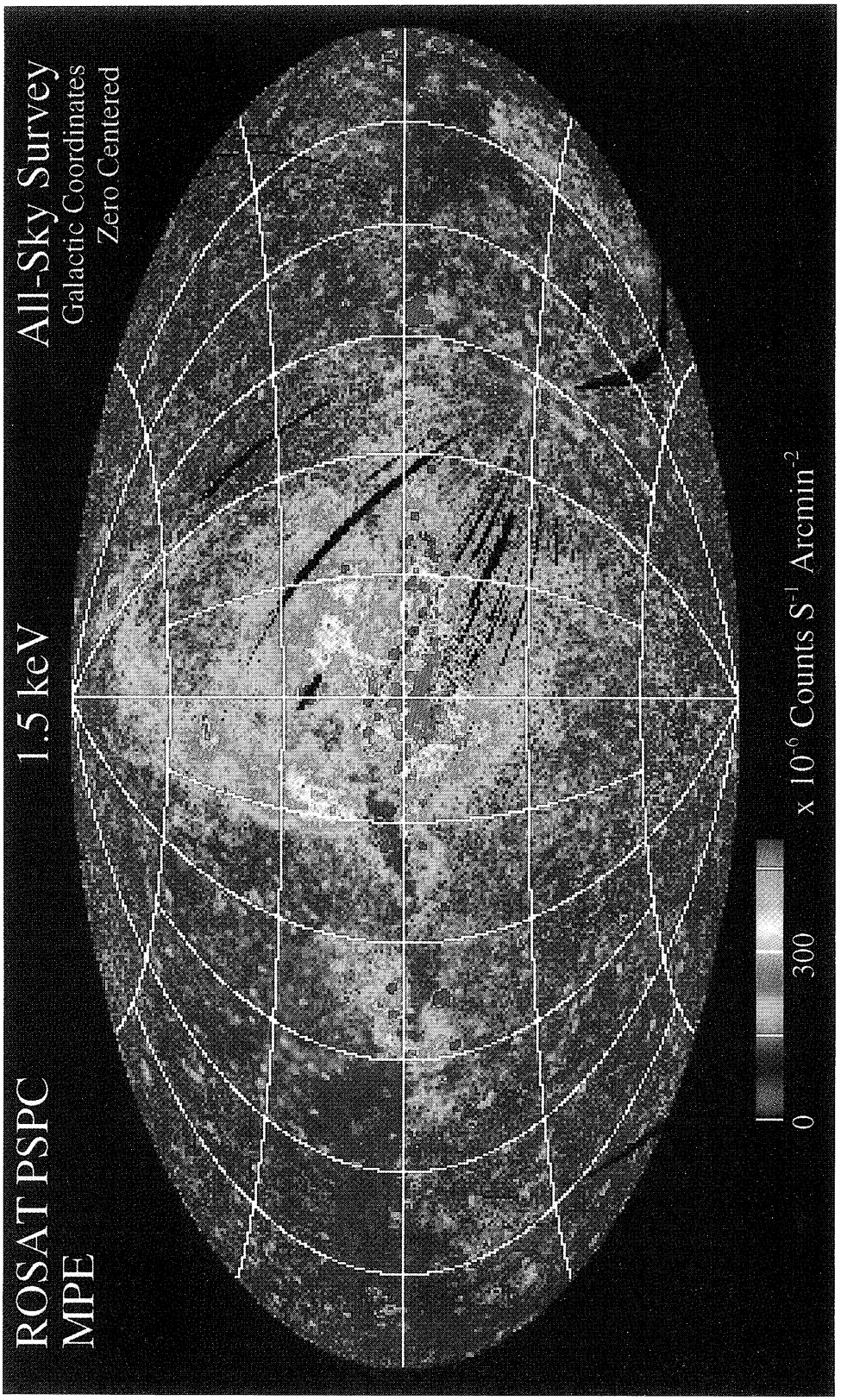

FIG. 5a

FIG. 5.—*ROSAT* XRT/PSPC maps for (*a*) the 1.5 keV band, (*b*) the $\frac{3}{4}$ keV band, and (*c*) $\frac{1}{4}$ band, in the same projection as Fig. 1

1995ApJ...454..643S

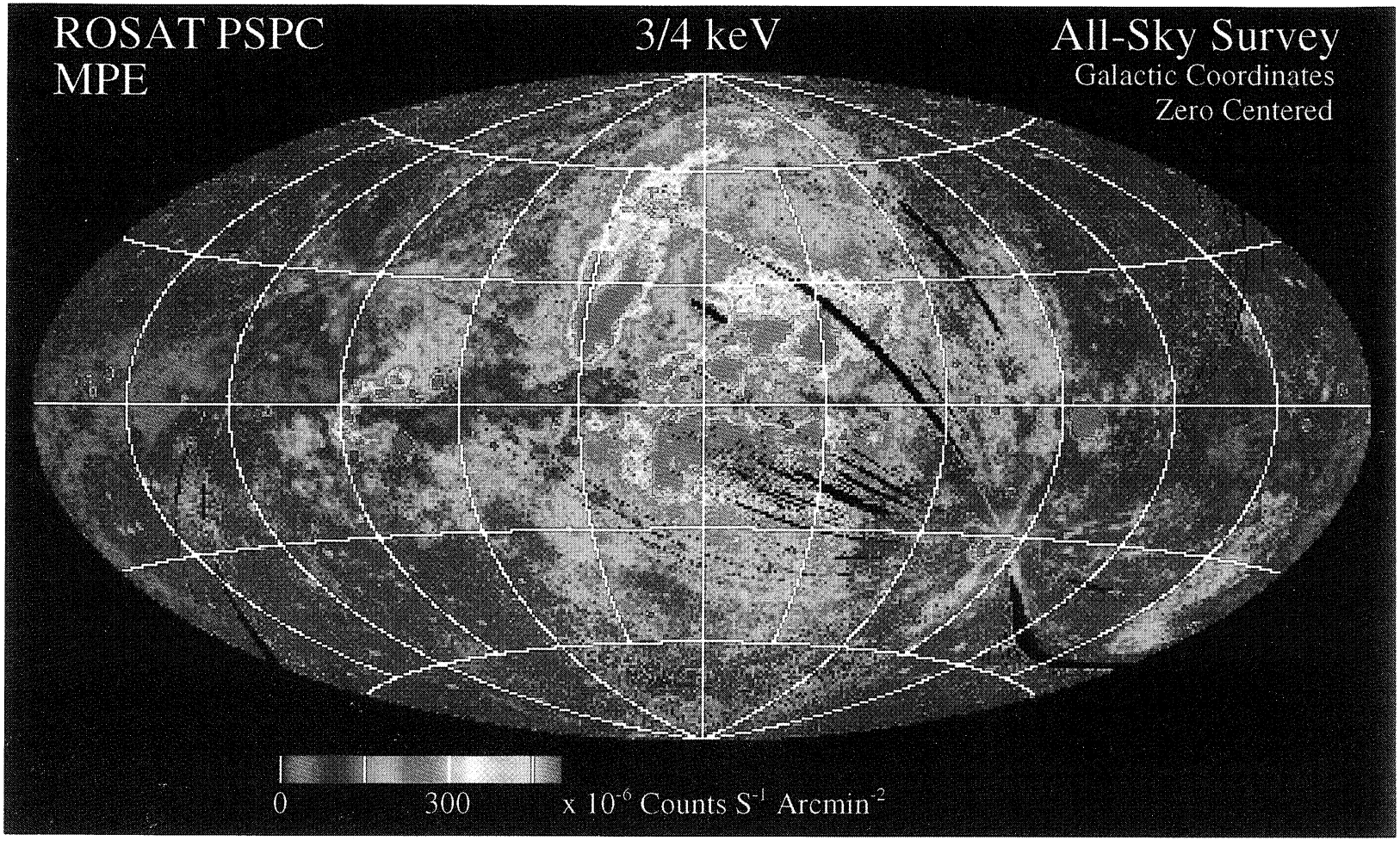

FIG. 5*b*

SNOWDEN et al. (see 455, 649)

PLATE 37

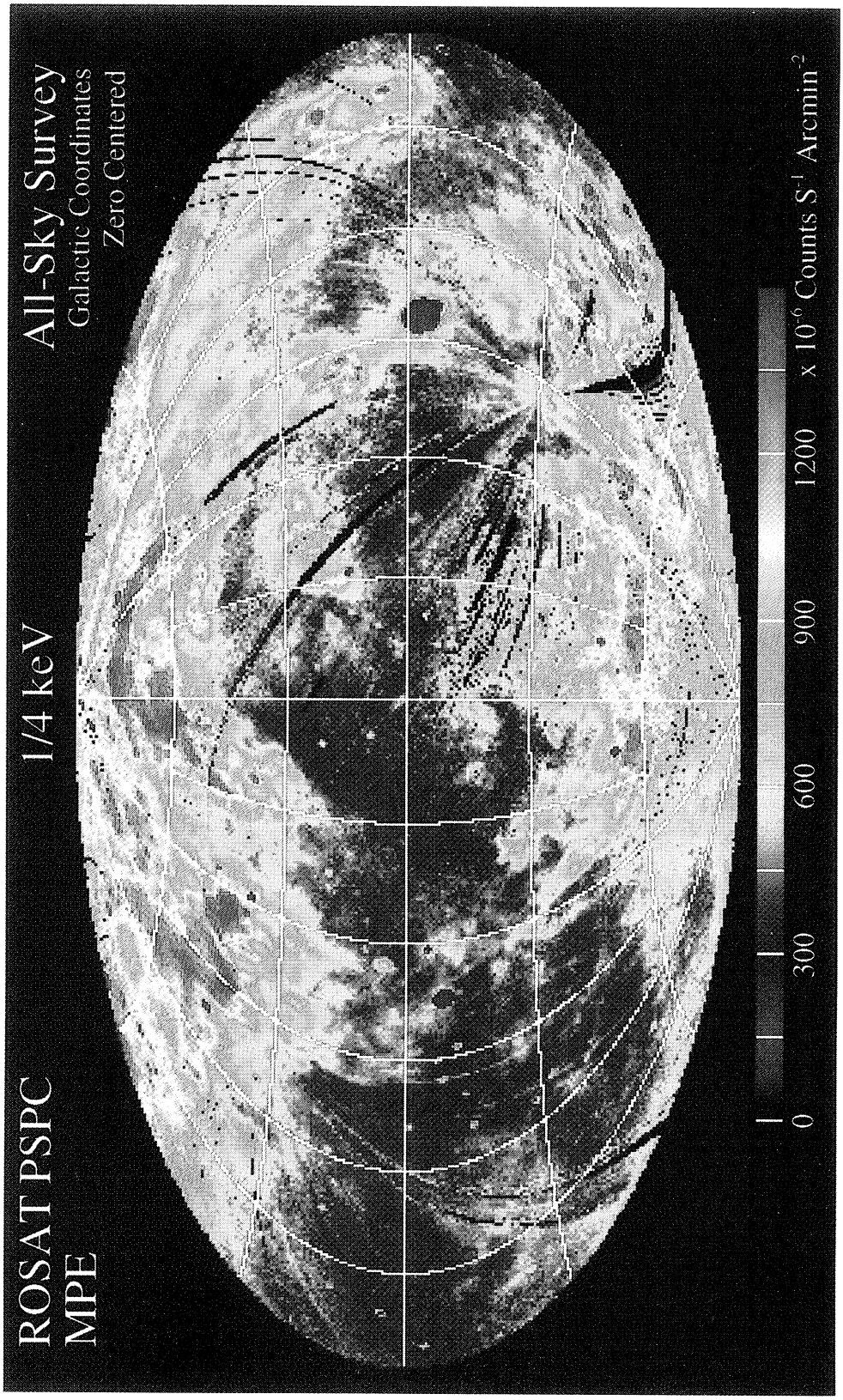

FIG. 5c

SNOWDEN et al. (see 455, 649)